A virtual testing strategy to determine effective yield criteria for porous pressure sensitive solids

Mahshid Ranjbar, Djordje Perić

Zienkiewicz Centre for Computational Engineering, College of Engineering, Swansea University, Swansea SA1 8EN, U. K.

Abstract

The aim of this work is to determine an effective yield criteria for porous pressure sensitive solids by employing a virtual testing strategy. The focus is on the pressure sensitivity typically displayed by geomaterials, such as sandstone. Virtual testing strategy is based on computational homogenisation approach following a unified variational formulation, which provides bounds on the effective material properties for a given choice of the Representative Volume Element (RVE). In order to estimate the effective properties of porous solid, the constitutive behaviour of continuum matrix is assumed to follow the standard Drucker-Prager elasto-plastic model. The computationally generated effective yield criteria for porous solids are obtained for various RVE choices and compared against the recently proposed analytical estimates for Drucker-Prager type solids and the SR4 constitutive model for soft rocks. The developed virtual testing strategy is applied to estimate the effective properties of a realistic rock sample, thus illustrating a wide range of potential applications.

Keywords: Multi-scale, Yield criterion, Computational homogenization, Virtual testing, Porous elasto-plastic materials

1. Introduction

In many practical situations it is necessary to consider several length scales in order to provide predictive modelling of a problem at hand. This situation arises,

Email address: d.peric@swansea.ac.uk (Djordje Perić)

for instance, in the area of geomechanical analysis of geological problems, where macro scale is commonly of the order of several kilometres, while relevant rock samples that characterise material behaviour typically measure several centimetres (see, e.g. [1; 2; 3]).

Traditional approach for such problems has relied on extensive experimental testing of material samples in order to provide a phenomenological constitutive model to be used in modelling at the macroscopic scale (see, e.g. [4; 5] and papers therein for recent contributions). However, designing an extensive experimental programme can be difficult as samples are often recovered at great expense and scarcely available. There is therefore a need to enhance experimental programme with computationally based techniques.

The present article discusses such a computational strategy with objective to construct a constitutive model that may be used in simulation of large scale problems. At the core of such computational strategy is a multiscale modelling methodology that relies on homogenisation of a suitable chosen Representative Volume Elements (RVEs). Since the basic principles for the multiscale modelling of heterogeneous materials were introduced (see [6; 7]), this methodology has proved to be a very effective way to deal with arbitrary physically non-linear and time dependent material behaviour at micro-level. During the last decade or so various approaches and techniques for the multiscale modelling and simulation of heterogeneous materials have been proposed. Among these we highlight the contributions by Ghosh et al. [8], Suquet and co-workers [9; 10], Feyel and Chaboche [11], Miehe and co-workers [12; 13; 14], Kouznetsova et al. [15], Ladevèze et al. [16], Terada and Kikuchi [17] and Ibrahimbegović and Markovič [18].

The aim of this work is to design a strategy to construct an effective yield criteria to be used in simulation at the macroscopic length scale. The effective yield criteria have been successfully constructed for porous materials with elasto-plastic von Mises matrix, starting with the classical work by Gurson [19], who first proposed an analytical yield criteria and flow rules for porous ductile media composed of von Mises matrix. Numerous publications have since been contributed on the topic as reported in a review article by Benzerga and Leblond [20], which discusses a wide variety of extensions of the original Gurson's model and its applications. Notable recent refinements and extensions of the original model are described in articles by Fritzen et al. [21], Monchiet and Bonnet [22], Ling et al. [23], Cazacu and Revil-Baudard [24] and El Ghezal and Doghri [25].

A significant practical and research interest exists in characterisation of porous

2

materials with pressure sensitive elasto-plastic matrix, which can often be encountered in geomaterials and solid polymers [1]. In early works Jeong [26] and Guo et al. [27] extend the Gurson's approach to determine an effective yield criteria for porous materials with elasto-plastic Coulomb and Drucker-Prager matrix, respectively. More recently, a substantial research effort has been invested to provide characterisation of porous materials with pressure sensitive matrix for different elasto-plastic constitutive laws and varied void configurations (see, for instance, [28], [29], [30], [21], [31], [32], [33] and [34], and references therein).

The objective of this work is to determine an effective yield criteria for porous solids with pressure sensitive matrix by employing a computational homogenisation approach following a unified variational formulation described in de Souza Neto and Feijoo [35] and Peric et al [36]. The formulation can be applied to arbitrary materials and provides bounds on the effective material properties for a given choice of the Representative Volume Element (RVE). It has already been successfully applied in prediction of yielding behaviour of ductile porous materials with pressure insensitive von Mises matrix (see [37], [38] and [39]). This article describes the first attempt to employ a generic computational homogenisation technique in constructing a macroscopic yield criterion for porous material with pressure sensitive Drucker-Prager type matrix.

The overall procedure has many similarities to the approach normally undertaken when performing experimental characterisation of the material behaviour and is therefore termed the *virtual testing strategy*. Main ingredients of a generic virtual testing strategy have recently been described by Zhang et al. [40] and Esmaeili et al. [41], and applied to the construction of the initial yield surface for sheet metal forming operations and heterogeneous composite with von Mises matrix, respectively.

The paper is organised as follows: The multi-scale constitutive framework is reviewed in Section 2 and the finite element approximation method provides in Section 3. Section 4 provides a brief summary of constitutive models considered in this work. Main steps of the virtual testing strategy are given in Section 5, while Section 6 provides numerical examples and includes comparative analysis against the results available in literature. Finally, the main conclusions and recommendations for future work are discussed.
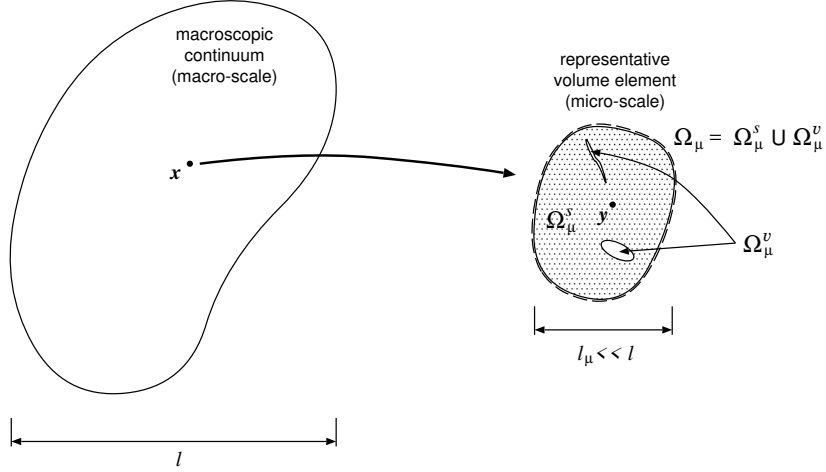
Figure 1. Macro-continuum with a locally attached micro-structure.

2. Homogenisation-based multi-scale constitutive theory

In order to provide a complete exposition of the virtual testing approach presented in this work, next two sections briefly describe variational basis and finite element approximation of the adopted multi-scale homogenisation methodology. For more details related to variational setting and finite element implementation we refer to our earlier articles [35], [36] and [42].

It is assumed from the outset that any material point x of the (macroscopic) continuum is associated with a local Representative Volume Element (RVE) whose domain Ω_μ, with boundary $\partial\Omega_\mu$, (see Figure 1), has a characteristic length, l_μ. Furthermore, it is assumed that the length l_μ is much smaller than the characteristic length, l, of the macro-continuum, thus ensuring the separation of scales, which is essential ingredient of the adopted family of the multi-scale methods. The domain Ω_μ of the RVE is assumed to consist in general of a solid part, Ω_μ^s, and a void part, Ω_μ^v:

$$\Omega_\mu = \Omega_\mu^s \cup \Omega_\mu^v. \tag{1}$$

For simplicity, in what follows, we shall consider only RVEs whose void part does not intersect the RVE boundary.

Fundamental assumption of the adopted multi-scale theory is that at any instant t, the strain tensor at an arbitrary point x of the macro-continuum is assumed to be the volume average of the microscopic strain tensor field, ε_μ, defined over Ω_μ :

4

$$\varepsilon(t) = \frac{1}{V_\mu} \int_{\Omega_\mu} \varepsilon_\mu(\boldsymbol{y}, t)\,\mathrm{d}V, \tag{2}$$

where V_μ is the volume of the RVE and

$$\varepsilon_\mu = \nabla^s \boldsymbol{u}_\mu, \tag{3}$$

where $\nabla^s \boldsymbol{u}_\mu$ denotes the symmetric gradient of the microscopic displacement field $\boldsymbol{u}_\mu$ of the RVE.

2.1. Kinematically admissible RVE displacement fields

By introducing expression (3) into equation (2) and making use of Green's theorem, it can easily be shown that the averaging relation (2) is equivalent to the following constraint on the displacement field of the RVE [35]:

$$\int_{\partial\Omega_\mu} \boldsymbol{u}_\mu \otimes_s \boldsymbol{n}\,\mathrm{d}A = \int_{\partial\Omega_\mu} \frac{1}{2}(\boldsymbol{u}_\mu \otimes \boldsymbol{n} + \boldsymbol{n} \otimes \boldsymbol{u}_\mu)\,\mathrm{d}A = V_\mu\,\varepsilon, \tag{4}$$

where $\boldsymbol{n}$ denotes the outward unit normal field on $\partial\Omega_\mu$.

It has proved convenient to split the displacement $\boldsymbol{u}_\mu$ into a sum

$$\boldsymbol{u}_\mu(\boldsymbol{y}, t) = \varepsilon(t)\,\boldsymbol{y} + \tilde{\boldsymbol{u}}_\mu(\boldsymbol{y}, t), \tag{5}$$

of a homogeneous strain displacement, $\varepsilon(t)\,\boldsymbol{y}$, and a *displacement fluctuation* field, $\tilde{\boldsymbol{u}}_\mu$. The constraint (4) is then equivalent to requiring that the space $\tilde{\mathscr{K}}_\mu$ of kinematically admissible displacement fluctuations of the RVE be a subspace of the *minimally constrained space of kinematically admissible displacement fluctuations*, $\tilde{\mathscr{K}}_\mu^*$:

$$\tilde{\mathscr{K}}_\mu \subset \tilde{\mathscr{K}}_\mu^* \equiv \left\{ \boldsymbol{v}, \text{ sufficiently regular} \,\Big|\, \int_{\partial\Omega_\mu} \boldsymbol{v} \otimes_s \boldsymbol{n}\,\mathrm{d}A = 0 \right\}. \tag{6}$$

Following the split (5) the microscopic strain (3) can be expressed as the sum

$$\varepsilon_\mu(\boldsymbol{y}, t) = \varepsilon(t) + \nabla^s \tilde{\boldsymbol{u}}_\mu(\boldsymbol{y}, t), \tag{7}$$

of a homogeneous strain field (coinciding with the macroscopic, average strain) and a field $\nabla^s \tilde{\boldsymbol{u}}_\mu$ that represents a fluctuation about the average.

5

2.2. Macroscopic stress, Hill-Mandel Principle and RVE equilibrium

In similarity to the above macroscopic strain definition (2), the macroscopic stress tensor, $\boldsymbol{\sigma}$, is defined as the volume average of the microscopic stress field, $\boldsymbol{\sigma}_\mu$, over the RVE:

$$\boldsymbol{\sigma}(t) = \frac{1}{V_\mu} \int_{\Omega_\mu} \boldsymbol{\sigma}_\mu(\boldsymbol{y}, t) \, \mathrm{d}V \, . \tag{8}$$

An essential concept that underlies models of the present type is the Hill-Mandel Principle of Macro-homogeneity [43; 44] which requires the macroscopic stress power to equal the volume average of the microscopic stress power for any kinematically admissible motion of the RVE. This is expressed by the equation

$$\boldsymbol{\sigma} : \dot{\boldsymbol{\varepsilon}}(t) = \frac{1}{V_\mu} \int_{\Omega_\mu} \boldsymbol{\sigma}_\mu : \dot{\boldsymbol{\varepsilon}}_\mu \, \mathrm{d}V \, , \tag{9}$$

that must hold for any kinematically admissible microscopic strain rate field, $\dot{\boldsymbol{\varepsilon}}_\mu$. The above is equivalent to the following variational equation:

$$\int_{\partial\Omega_\mu} \boldsymbol{t} \cdot \boldsymbol{\eta} \, \mathrm{d}A = 0, \quad \int_{\Omega_\mu} \boldsymbol{b} \cdot \boldsymbol{\eta} \, \mathrm{d}V = 0 \quad \forall \boldsymbol{\eta} \in \tilde{\mathcal{K}}_\mu \, , \tag{10}$$

in terms of the RVE boundary traction and body force fields denoted, respectively, $\boldsymbol{t}$ and $\boldsymbol{b}$.

The variational equilibrium statement for the RVE is then given by

$$\int_{\Omega_\mu} \boldsymbol{\sigma}_\mu : \nabla^s \boldsymbol{\eta} \, \mathrm{d}V = 0 \quad \forall \boldsymbol{\eta} \in \tilde{\mathcal{K}}_\mu \, . \tag{11}$$

Further, we assume that at any time t the stress at each point $\boldsymbol{y}$ of the RVE is delivered by a generic constitutive functional $\mathfrak{S}_{\boldsymbol{y}}$ of the strain history $\varepsilon_\mu^t(\boldsymbol{y})$ at that point up to time t:

$$\boldsymbol{\sigma}_\mu(\boldsymbol{y}, t) = \mathfrak{S}_{\boldsymbol{y}}\big(\varepsilon_\mu^t(\boldsymbol{y})\big). \tag{12}$$

This constitutive assumption, together with the equilibrium equation (11) leads to the definition of the RVE equilibrium problem which consists in finding, for a given macroscopic strain ε (a function of time), a displacement fluctuation function $\tilde{\boldsymbol{u}}_\mu \in \tilde{\mathcal{K}}_\mu$ such that

$$\int_{\Omega_\mu^s} \mathfrak{S}_{\boldsymbol{y}}\left\{ \left[\varepsilon(t) + \nabla^s \tilde{\boldsymbol{u}}_\mu(\boldsymbol{y}, t) \right]^t \right\} : \nabla^s \boldsymbol{\eta} \, \mathrm{d}V = 0 \quad \forall \boldsymbol{\eta} \in \tilde{\mathcal{K}}_\mu \, . \tag{13}$$

6

2.3. Characterisation of the multi-scale constitutive model

The general multi-scale constitutive model in the present context is defined as follows. For a given macroscopic strain history, we must firstly solve the RVE equilibrium problem defined by (13). With the solution $\tilde{u}_\mu$ at hand, the macroscopic stress tensor is determined according to the averaging relation (8), i.e., we have

$$\boldsymbol{\sigma}(t) = \mathfrak{S}(\varepsilon^t) \equiv \frac{1}{V_\mu} \int_{\Omega_\mu} \mathfrak{S}_{\boldsymbol{y}} \left\{ \left[\boldsymbol{\varepsilon} + \nabla^s \tilde{\boldsymbol{u}}_\mu \right]^t \right\} \mathrm{d}V, \tag{14}$$

where $\mathfrak{S}$ denotes the resulting (homogenised) macroscopic constitutive functional.

2.4. The choice of kinematical constraints

The characterisation of a multi-scale model of the present type is completed with the choice of a suitable space of kinematically admissible displacement fluctuations, $\tilde{\mathcal{K}}_\mu \subset \tilde{\mathcal{K}}_\mu^*$. In general, different choices lead to different macroscopic response functional. The following choices are as:

2.4.1. Linear boundary displacements (or zero boundary fluctuations) model:

$$\tilde{\mathcal{K}}_\mu = \tilde{\mathcal{K}}_{\mathrm{lin}} \equiv \left\{ \boldsymbol{v}, \text{ sufficiently regular} \, | \, \boldsymbol{v}(\boldsymbol{y}) = 0 \, \forall \, \boldsymbol{y} \in \partial\Omega_\mu \right\}. \tag{15}$$

The displacements of the boundary of the RVE for this class of models are fully prescribed as

$$\boldsymbol{u}_\mu(\boldsymbol{y}) = \boldsymbol{\varepsilon} \, \boldsymbol{y} \quad \forall \boldsymbol{y} \in \partial\Omega_\mu. \tag{16}$$

2.4.2. Periodic boundary fluctuations. This assumption is typically associated with the description of media with periodic microstructure. The macrostructure in this case is generated by the periodic repetition of the RVE [10]. For simplicity, we will focus the description on two-dimensional problems and we shall follow the notation adopted by Michel et al. [10]. In this case, each pair i of sides consists of equally sized subsets

$$\Gamma_i^+ \quad \text{and} \quad \Gamma_i^- \tag{17}$$

of $\partial\Omega_\mu$, with respective unit normals

$$\boldsymbol{n}_i^+ \quad \text{and} \quad \boldsymbol{n}_i^-, \tag{18}$$

such that

$$\boldsymbol{n}_i^- = -\boldsymbol{n}_i^+. \tag{19}$$

7

A one-to-one correspondence exists between the points of Γ_i^+ and Γ_i^-. That is, each point $\boldsymbol{y}^+ \in \Gamma_i^+$ has a corresponding pair $\boldsymbol{y}^- \in \Gamma_i^-$. The key kinematical constraint for this class of models is that the displacement fluctuation must be periodic on the boundary of the RVE. That is, for each pair $\{\boldsymbol{y}^+, \boldsymbol{y}^-\}$ of boundary material points we have

$$\tilde{\boldsymbol{u}}_\mu(\boldsymbol{y}^+, t) = \tilde{\boldsymbol{u}}_\mu(\boldsymbol{y}^-, t). \tag{20}$$

Accordingly, the space $\tilde{\mathscr{K}}_\mu$ is defined as

$$\tilde{\mathscr{K}}_\mu = \tilde{\mathscr{K}}_{\text{per}} \equiv \left\{ \tilde{\boldsymbol{u}}_\mu, \text{suff.reg.} \mid \tilde{\boldsymbol{u}}_\mu(\boldsymbol{y}^+, t) = \tilde{\boldsymbol{u}}_\mu(\boldsymbol{y}^-, t) \, \forall \, \text{pairs} \{\boldsymbol{y}^+, \boldsymbol{y}^-\}. \right\} \tag{21}$$

2.4.3. The minimally constrained (or uniform boundary traction) model:

$$\tilde{\mathscr{K}}_\mu \equiv \tilde{\mathscr{K}}_\mu^*. \tag{22}$$

It can be shown [35] that the distribution of stress vector on the RVE boundary, associated with the minimal kinematic constraint, satisfies

$$\boldsymbol{\sigma}_\mu(\boldsymbol{y}, t)\, \boldsymbol{n}(\boldsymbol{y}) = \boldsymbol{\sigma}(t)\, \boldsymbol{n}(\boldsymbol{y}) \quad \forall \boldsymbol{y} \in \partial \Omega_\mu. \tag{23}$$

Similarly to the linear boundary displacements assumption, there are no restrictions on the geometry of the RVE for this choice of the RVE constraint.

It should be pointed out that the use of different boundary conditions for a given RVE produces, in general, different estimates of the corresponding macroscopic constitutive response. The general rule, which follows after a careful mathematical arguments based on variational calculus (see, for instance, Peric et al [36] and references therein), is that the linear boundary displacement (most kinematically constrained) produces the upper bound solution to the microscopic equilibrium problem, followed in order of decreasing stiffness, by the periodic displacement fluctuation and the uniform boundary traction model, which produces lower bound estimate that is associated with the most compliant (least kinematically constrained) boundary condition.

3. Finite element approximation

This section provides a brief description of the computational implementation of multi-scale constitutive methodology described in Section 2 within a non-linear

finite element framework. At the outset, it is assumed that the constitutive behaviour at the RVE level is described by conventional internal variable-based dissipative constitutive laws, such as classical models of elasto-plasticity and elasto-viscoplasticity. Numerical approximations to the initial value problem defined by the constitutive equations of the model are usually obtained by Euler-type difference schemes. For a typical time (or pseudo-time) interval $\left[t^n, t^{n+1} \right]$, and given set of $\boldsymbol{\alpha}^n$ of internal variables at t^n, the stress $\boldsymbol{\sigma}_\mu^{n+1}$ at t^{n+1} is a function of the prescribed strain ε_μ^{n+1} at t^{n+1} (see, for instance, de Souza Neto et al [45] for a detailed account of procedures of this kind in the context of plasticity and visco-plasticity). The stress update procedure can be symbolically represented as

$$\boldsymbol{\sigma}_\mu^{n+1} = \hat{\boldsymbol{\sigma}}_y(\varepsilon_\mu^{n+1}; \boldsymbol{\alpha}^n), \qquad (24)$$

where $\hat{\boldsymbol{\sigma}}_y$ denotes the integration algorithm-related implicit incremental constitutive function at the point of interest, $\boldsymbol{y}$.

The homogenised constitutive function defined in (14), can now be expressed in its incremental form as:

$$\boldsymbol{\sigma}^{n+1} = \hat{\boldsymbol{\sigma}}(\varepsilon^{n+1}; \bar{\boldsymbol{\alpha}}^n) \equiv \frac{1}{V_\mu} \int_{\Omega_\mu} \hat{\boldsymbol{\sigma}}_y(\varepsilon^{n+1} + \nabla^s \tilde{\boldsymbol{u}}_\mu^{n+1}; \boldsymbol{\alpha}^n) \, dV, \qquad (25)$$

where $\bar{\boldsymbol{\alpha}}^n$ denotes the field of internal variable sets over Ω_μ at time t_n and $\tilde{\boldsymbol{u}}_\mu^{n+1}$ is the displacement fluctuation field of the RVE at t^{n+1}, which is obtained as the solution of the time-discrete version of equilibrium problem (13):

$$\int_{\Omega_\mu^s} \hat{\boldsymbol{\sigma}}_y(\varepsilon^{n+1} + \nabla^s \tilde{\boldsymbol{u}}_\mu^{n+1}; \boldsymbol{\alpha}^n) : \nabla^s \boldsymbol{\eta} \, dV = 0 \quad \forall \boldsymbol{\eta} \in \tilde{\mathcal{K}}_\mu. \qquad (26)$$

3.1. Finite element discretisation and solution

Following a standard procedure, the finite element approximation to problem (26) for a given discretisation h consists in determining the unknown vector $\tilde{\boldsymbol{u}}_\mu^{n+1} \in \tilde{\mathcal{K}}_\mu^h$ of global nodal displacement fluctuations such that

$$G^h(\tilde{\boldsymbol{u}}_\mu^{n+1}) \equiv \left\{ \int_{\Omega_\mu^h} \mathbf{B}^T \hat{\boldsymbol{\sigma}}_y(\varepsilon^{n+1} + \mathbf{B} \, \tilde{\boldsymbol{u}}_\mu^{n+1}) \, dV \right\} \cdot \boldsymbol{\eta} = 0 \quad \forall \boldsymbol{\eta} \in \tilde{\mathcal{K}}_\mu^h, \qquad (27)$$

where Ω_μ^h denotes the discretised RVE domain, $\mathbf{B}$ the global strain-displacement matrix (or discrete symmetric gradient operator), ε^{n+1} is the fixed (given) array

of macroscopic engineering strains at t^{n+1} , $\hat{\boldsymbol{\sigma}}_y$ is the functional that delivers the finite element array of stress components, $\boldsymbol{\eta}$ denotes global vectors of nodal virtual displacements of the RVE and $\tilde{\mathscr{K}}_\mu^h$ is the finite-dimensional space of virtual nodal displacement vectors associated with the finite element discretisation h of the domain Ω_μ.

The solution to the non-linear problem (27) is commonly undertaken by the Newton-Raphson iterative scheme, whose typical iteration $(k+1)$ consists in solving the linearised form,

$$\left[\mathbf{F}^{(k)} + \mathbf{K}^{(k)} \, \delta\tilde{\boldsymbol{u}}_\mu^{(k+1)} \right] \cdot \boldsymbol{\eta} \; = \; 0 \quad \forall \boldsymbol{\eta} \in \tilde{\mathscr{K}}_\mu^h \,, \tag{28}$$

for the unknown iterative nodal displacement fluctuations vector, $\delta\tilde{\boldsymbol{u}}_\mu^{(k)} \in \tilde{\mathscr{K}}_\mu^h$ where

$$\mathbf{F}^{(k)} \equiv \int_{\Omega_\mu^h} \mathbf{B}^T \hat{\boldsymbol{\sigma}}_y (\boldsymbol{\varepsilon}^{n+1} + \mathbf{B} \, \tilde{\boldsymbol{u}}_\mu^k) \, \mathrm{d}V \,, \tag{29}$$

and

$$\mathbf{K}^{(k)} \equiv \int_{\Omega_\mu^h} \mathbf{B}^T \mathbf{D}^{(k)} \mathbf{B} \, \mathrm{d}V \tag{30}$$

is the tangent stiffness matrix of the RVE with

$$\mathbf{D}^{(k)} \equiv \left. \frac{\mathrm{d}\hat{\boldsymbol{\sigma}}_y}{\mathrm{d}\boldsymbol{\varepsilon}} \right|_{\boldsymbol{\varepsilon} = \boldsymbol{\varepsilon}^{n+1} + \mathbf{B}\tilde{\boldsymbol{u}}_\mu^{n+1}} \tag{31}$$

denoting the consistent constitutive tangent matrix field over the RVE domain. In the above the bracketed superscript denotes the Newton iteration number. With the solution $\delta\tilde{\boldsymbol{u}}_\mu^{(k)}$ at hand, the new guess $\tilde{\boldsymbol{u}}_\mu^{(k)}$ for the displacement fluctuation at t_{n+1} is obtained according to the Newton-Raphson update formula

$$\tilde{\boldsymbol{u}}_\mu^{(k+1)} = \tilde{\boldsymbol{u}}_\mu^{(k)} + \delta\tilde{\boldsymbol{u}}_\mu^{(k+1)} \,. \tag{32}$$

It should be noted that under the assumption of linear boundary displacements, the solution of problem (28) follows the conventional route of general linear solid mechanics problems, with the fluctuations degrees of freedom of the boundary fully prescribed as zero. For the periodic and uniform tractions boundary condition models, however, the kinematic boundary conditions of the RVE are non-conventional. For details of implementation of different boundary conditions within the described variational framework under both small and large strain conditions we refer to our earlier publications [36] and [42], respectively.

10

4. Constitutive models

Pressure sensitive elasto-plastic materials are widely encountered, both as naturally occurring (rocks, soils) and artificially designed (concrete, solid polymers). Hence, characterisation of constitutive behaviour of such materials has attracted a significant research and practical interest. This section briefly reviews three elasto-plastic yield criteria for pressure sensitive materials, starting first with a classical Drucker-Prager yield criterion, and then discusses the constitutive description of two yield criteria that have more recently been proposed to characterise behaviour of porous materials with pressure sensitive matrix.

4.1. Standard Drucker-Prager model

The classical Drucker–Prager yield criterion is a simple extension of the von Mises yield criterion, in which pressure sensitivity is introduced through a linear dependence of the von Mises deviatoric stress on the hydrostatic pressure. Due to its simplicity the Drucker-Prager yield criterion has often been used as a first approximation of pressure sensitive elasto-plastic behaviour in wide range of materials such as soils, rock, concrete, solid polymers, foams, etc. Its mathematical representation is given as,

$$\Phi(\boldsymbol{\sigma}, c) = q + \frac{\tan\phi}{\sqrt{3}} p(\boldsymbol{\sigma}) - c \tag{33}$$

where, $q = \sqrt{J_2(\boldsymbol{s}(\boldsymbol{\sigma}))}$, in which $J_2(\boldsymbol{s}) = \frac{1}{2}\boldsymbol{s} : \boldsymbol{s}$ is the second invariant of the deviatoric stress $\boldsymbol{s}$, $\boldsymbol{s} = \boldsymbol{\sigma} - p(\boldsymbol{\sigma})\boldsymbol{I}$ is the deviatoric stress tensor and $p = \frac{1}{3}\text{tr}[\boldsymbol{\sigma}]$ is the hydrostatic pressure. Here ϕ and c denote the frictional angle and cohesion, respectively, which need to be determined through experimental procedure.

4.2. Constitutive model for porous solids with Drucker-Prager elasto-plastic matrix

Constitutive description of porous materials with the pressure sensitive elasto-plastic matrix has received some attention. In early work Guo et al. [27] extend the Gurson's approach to determine an effective yield criteria for porous materials with elasto-plastic Drucker-Prager matrix. More recently, an increased research effort has been invested to provide characterisation of porous materials with pressure sensitive elasto-plastic matrix and varied void configurations (see, for instance, [28], [29], [30], [21], [31] and [32], and references therein). In particular, Shen et al [33] provide a convenient mathematical expression of the macroscopic yield

11

criterion for porous material with Drucker-Prager elasto-plastic matrix and spherical voids. The macroscopic yield surface is expressed as,

$$\bar{q} = \left\{ \left(-2f \cosh\left(\frac{2M + \text{sign}(\bar{p})}{2M}\ln\left(1 - 3M\bar{p}\right)\right) + 1 + f^2 \right)\left[1 - \frac{3M\bar{p}}{(1-f)}\right]^2 \right\}^{\frac{1}{2}} \quad (34)$$

where $M = \dfrac{\tan(\phi)}{\sqrt{3}}$, f = void ratio , $\bar{q}$ and $\bar{p}$ are, respectively, deviatoric and hydrostatic stresses normalised by $\sqrt{3}\,c$. We point out that a recent paper by Shen et al [34] provides an updated version of the macroscopic yield criterion for porous material Drucker-Prager elasto-plastic matrix, which is together with the above expression (34), employed in comparative analysis of numerical results provided in Section 6.

4.3. The soft rock SR4 model

The SR4 is a generic elastic-plastic critical state constitutive model originally designed to describe porous elasto-plastic materials, such as sandstone [46]. The SR4 has proved very successful in description of much larger class of geomaterials and in this work it is employed to the describe macroscopic behaviour of heterogeneous elasto-plastic materials with pressure sensitive matrix.

It is defined in the $p - q$ plane with two functions that intersect at the point of maximum deviatoric stress.

The shear side is defined using the SR3 surface [47], whereas the compression side is defined by the elliptical function of the standard Cam-Clay model [48; 49]. Its mathematical representation is given as

$$\Phi(\boldsymbol{\sigma}, \varepsilon_p^v) = g(\theta, p)q + (p - p_t)\tan\phi\left(\frac{p - p_c}{p_t - p_c}\right)^{\frac{1}{n}} \quad (35)$$

$$\Phi_{\text{cap}} = (gq)^2 - M_\phi^2 p_{\phi_{\text{crit}}}^2\left[1 - \frac{(p_{\phi_{\text{crit}}} - p)^2}{(p_{\phi_{\text{crit}}} - p_c)^2}\right] = 0 \quad (36)$$

where p_t is the tensile intercept of the yield surface with the hydrostatic axis, p_c is the pre-consolidation pressure or compressive intercept of the yield surface with the hydrostatic axis, $p_{\phi_{\text{crit}}}$ is the effective mean stress at q_{crit} value, ε_p^v is the plastic volumetric strain, M_ϕ is the slope of the line that intersects both the origin of the

12

$p - q$ space and the yield surface in q_{crit} value, n is material constant that defines the shape of the yield surface in the $p - q$ plane, θ is the Lode angle and $g(\theta, p)$ is a function that controls the shape of the yield surface in the deviatoric plane and is computed as

$$g(\theta, p) = \left[\frac{1}{1 - \beta^\pi(p)} (1 + \beta^\pi(p)\sin(3\theta)) \right]^{N^\pi}. \tag{37}$$

Here N^π is a deviatoric plane shape material constant and $\beta^\pi(p)$ is a function defined as

$$\beta^\pi(p) = \beta_0^\pi \exp(\beta_1^\pi p \frac{p_{co}}{p_c}) \tag{38}$$

in which β_0^π and β_1^π are material constants and p_{co} is the initial pre-consolidation pressure (corresponding to uncompressed and undamaged material). In order to match the SR4 yield surface with the Drucker-Prager yield shape the g factor is taken as 1 by setting $\beta_0^\pi = 0$. It should be noted that in order to provide accurate representation of material behaviour the SR4 yield surface is often combined with a separate flow surface, thus defining a non-associative elasto-plastic constitutive law.

5. Virtual testing strategy

This section discusses a computational strategy, which is designed with an objective to construct a constitutive model that may be used in simulation of macroscopic scale problems. The overall procedure has many similarities with the approach normally undertaken when performing experimental characterisation of the material behaviour and is therefore termed the *virtual testing strategy*. Main ingredients of a generic virtual testing strategy have recently been described by Zhang et al. [40] and Esmaeili et al. [41], and applied to the construction of the initial yield surface for sheet metal forming operations and heterogeneous composite with von Mises matrix, respectively. In this context notable are also recent contributions by Rodrigo et al. [39], Cao et al. [2] and Ahmed et al. [50].

At the core of a virtual testing strategy is a multiscale modelling methodology that relies on homogenisation of a suitably chosen Representative Volume Elements (RVEs). This work employs a computational homogenisation approach that follows a unified variational formulation described in [35] and [36], which is briefly summarised in Sections 2 and 3. The formulation can be applied to arbitrary

13

materials and has a very useful feature that it provides bounds on the effective material properties for a given choice of the Representative Volume Element (RVE).

It should be observed that a virtual testing strategy based on such an RVE formulation has already been successfully applied in prediction of yielding behaviour of ductile porous materials with pressure insensitive von Mises matrix (see [37], [38] and [39]). This article describes the first attempt to employ a virtual testing strategy to construct a macroscopic yield criterion for porous material with pressure sensitive Drucker-Prager type matrix. As will be discussed below, the construction of an effective yield surface for pressure sensitive materials presents unique challenges not faced when employing the von Mises type materials and requires very careful and judicious choices when defining an effective constitutive law.

The main steps of the virtual testing strategy used in this work are illustrated in Figure 2. It should be noted that in order to describe the behaviour of practically relevant problems, two strategies may be distinguished that correspond to different length scales of the problem at hand. In strategy A an effective constitutive law obtained within the virtual testing strategy is applied directly in simulation of a macroscopic scale problem. In Strategy B the virtual testing involves an additional step that provides an effective constitutive law for the behaviour of material at mesoscopic scale. Strategy B is employed when significant heterogenities are present at multiple length scales of material. Both strategies will be discussed in more detail in Sections 5.1-5.3 .

5.1. RVE choice

Two unit cube RVEs are considered for all numerical results generated in Section 6: (i) A cube with a single spherical void at the centre, and (ii) a cube with eight variable size randomly distributed spherical voids. The void ratio V_μ^v is kept constant at 10% for all numerical examples. This represents a void volume fraction typical for sandstone. The RVEs are discretised by eight noded hexahedral elements. RVEs are shown in Figures 3(a) and 3(b), with cuts through discretised finite element meshes with void ratio $f = 10\%$ depicted in Figures 3(c) and 3(d). The RVE shown in Figure 3(c) is discretised with 106636, while the one in Figure 3(d) is discretised with 1567766 hexahedral elements.
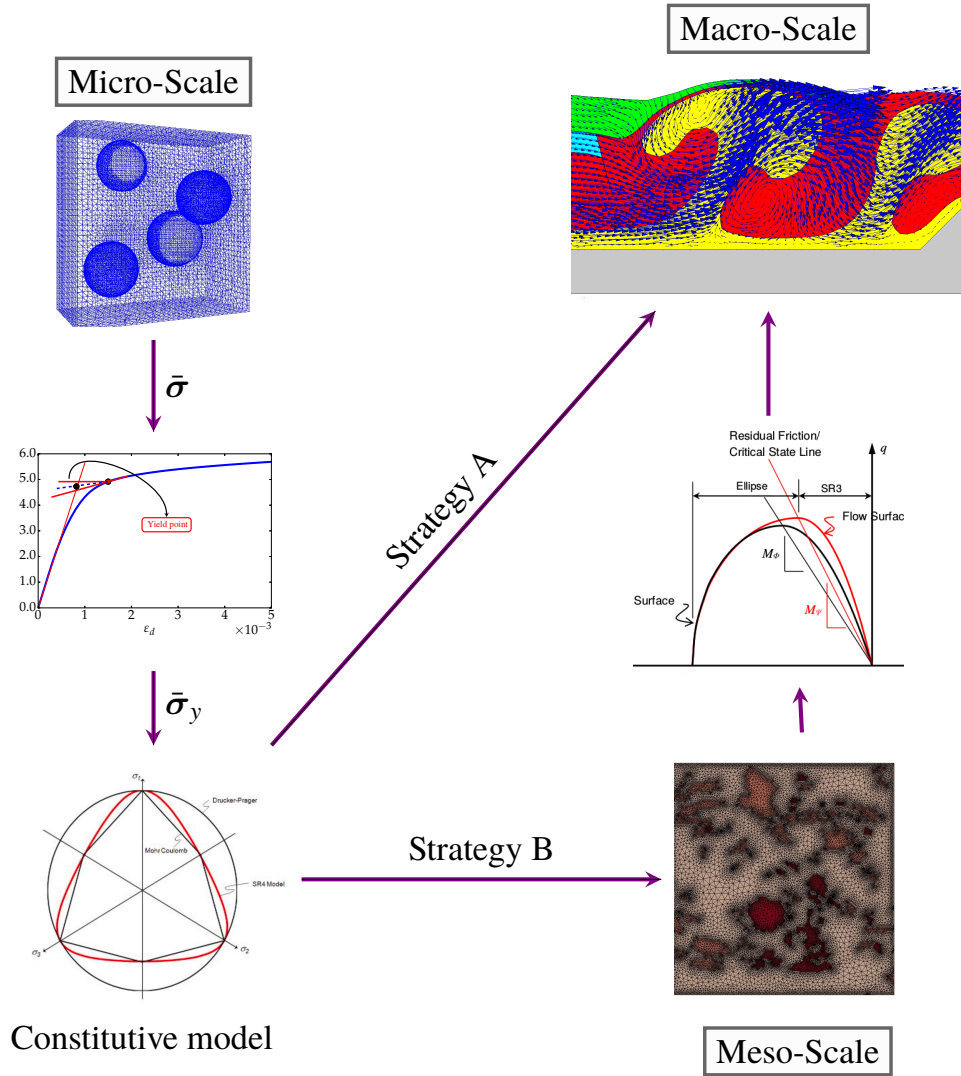
14

Figure 2. Virtual testing strategy.

5.2. Yield criterion estimate

A crucial aspect of the described virtual testing strategy is identification of the yield stress under different loading conditions. For the RVEs composed of the pressure insensitive von Mises type elasto-plastic material, plastic collapse of the RVE is considered to have occurred when no changes in macroscopic (homogenised) stress
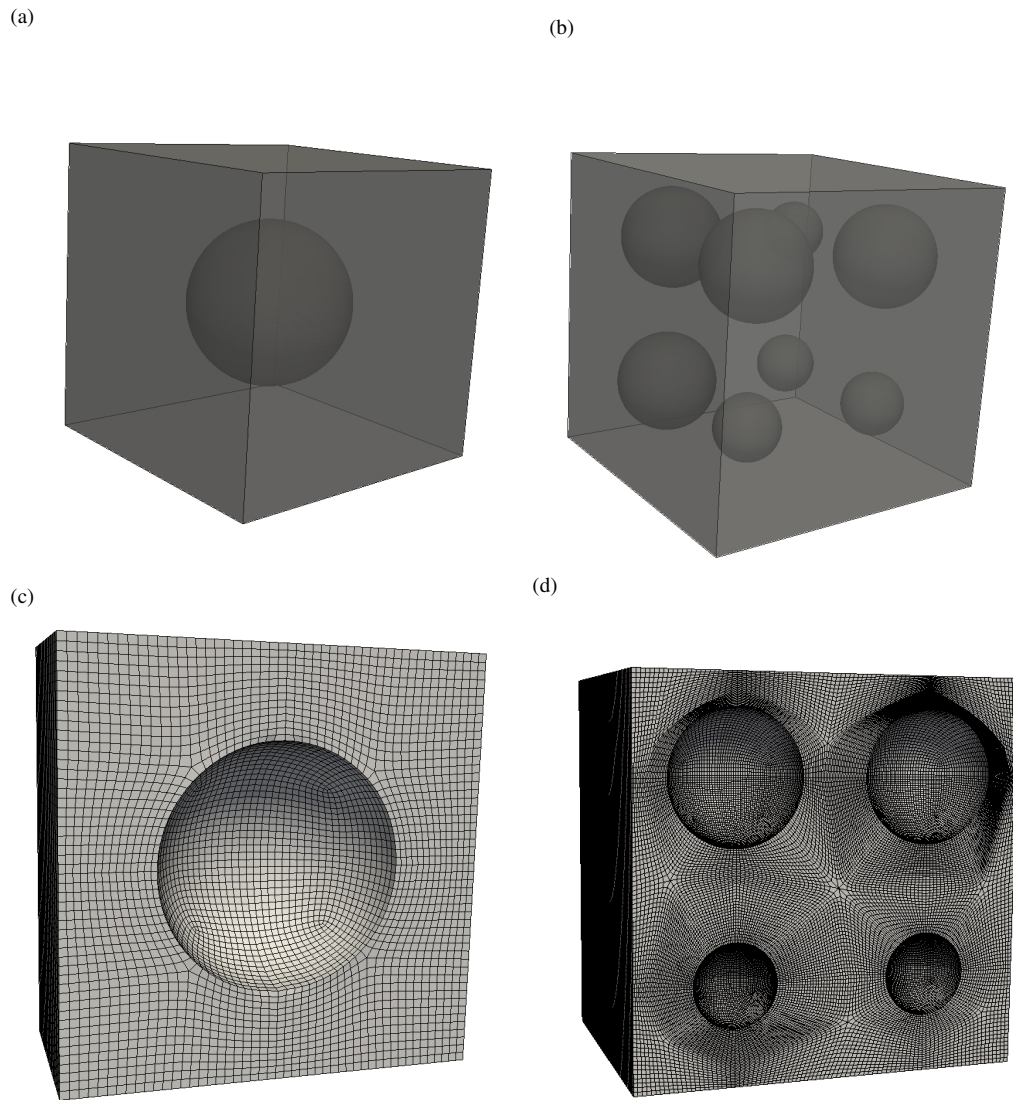
(a)   (b)

(c)   (d)

Figure 3. RVE geometries and finite element models: (a) and (c) single void RVE; (b) and (d) RVE with multiple voids.

are observed for the increasing load factor. This procedure allows a straightforward estimate of the von Mises and hydrostatic components of the macroscopic collapse stress, which define a yield surface point (see [37], [38] and [39] for details of the methodology and examples).

For the RVEs composed of pressure sensitive elasto-plastic materials this has

16

proved to be a more challenging task. While the above procedure is applicable for tensile and shear side of the $p - q$ diagram, the pressure sensitivity of material does not allow a simple estimate of the yield stress at the compressive side of the $p - q$ diagram. In order to overcome the ambiguity and in the spirit of the described virtual testing strategy, in this work the Casagrande method [51] is employed to identify the yield point in $p - \varepsilon_v$ and $q - \varepsilon_d$ diagrams for all loading conditions, where ε_v and ε_d are volumetric and deviatoric strain, respectively. It should be noted that the Casagrande method has originally been proposed to predict the pre-consolidation pressure of soil samples and is nowadays also commonly employed to estimate first yield stress during experimental procedure involving soil and rock materials. Graphical illustration of the procedure is given in Figure 4. Within the classical Casagrande method the yield stress is identified at the intersect of the linear virgin elastic loading curve and the bisect of a horizontal and tangent drawn at the point on the stress-strain response curve of maximum curvature (see Figure 4). This procedure has proved essential in identifying yield stress for the cases when transition between elastic and plastic deformation regime is slow, resulting in a gradual change of slope of the stress-strain curve.
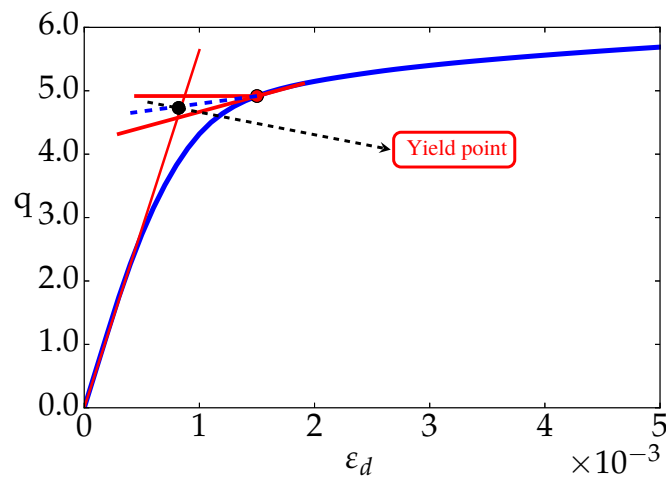
Figure 4. Illustration of the Casagrande method.

17

5.3. RVE loading

The loading programme consists in prescribing a macroscopic strain path

$$\varepsilon(\gamma) = \gamma\bar{\varepsilon} \tag{39}$$

where γ where is the loading parameter and $\bar{\varepsilon}$ is the strain imposed on the RVEs. In order to construct a yield criterion in the stress space the macroscopic strain $\bar{\varepsilon}$ is varied according to the following rule:

$$\bar{\varepsilon} = \alpha_1 \begin{bmatrix} \frac{1}{200} & 0 & 0 \\ 0 & \frac{1}{200} & 0 \\ 0 & 0 & \frac{1}{200} \end{bmatrix} + \sqrt{1-\alpha_1^2} \begin{bmatrix} 0 & \frac{1}{200} & \frac{1}{200} \\ \frac{1}{200} & 0 & \frac{1}{200} \\ \frac{1}{200} & \frac{1}{200} & 0 \end{bmatrix} \tag{40}$$

where $\alpha_1 \in [-1, 0]$ for the compressive side of the $p - q$ diagram, while for the tension side the following expression is employed

$$\bar{\varepsilon} = \alpha_2 \begin{bmatrix} \frac{1}{1000} & 0 & 0 \\ 0 & \frac{1}{1000} & 0 \\ 0 & 0 & \frac{1}{1000} \end{bmatrix} + \sqrt{1-\alpha_2^2} \begin{bmatrix} 0 & \frac{1}{200} & \frac{1}{200} \\ \frac{1}{200} & 0 & \frac{1}{200} \\ \frac{1}{200} & \frac{1}{200} & 0 \end{bmatrix} \tag{41}$$

in which $\alpha_2 \in [0, 1]$. Note that $\alpha_1 = 0$ and $\alpha_2 = 0$ correspond to a pure shear direction, whereas $\alpha_1 = -1$ corresponds to triaxial compression, while $\alpha_2 = 1$ defines triaxial tension loading. By varying parameters α_1 and α_2 a sufficient number of yield points can be determined to allow an accurate yield surface to be constructed.

6. Numerical results

Virtual testing strategy described in Section 5 is employed in this Section to construct a macroscopic yield surface for porous pressure sensitive material with Drucker-Prager elasto-plastic matrix. Numerical results are obtained by using an in-house implicit finite element code described in [45] and the commercial finite element software ParaGeo [52] that relies on explicit solution strategy. Numerically generated results are compared against the analytical estimates of yield criteria given by expressions in Section 4.

In order to generate numerical results the following set of material constants has been selected: Young's modulus, $E = 3000$ MPa and Poisson's ratio, $\nu = 0.3$. Two friction angles are considered, $\phi = 16.7°$ and $\phi = 30.2°$, while cohesion is taken as $c = 1$ MPa.

(a)   (b)
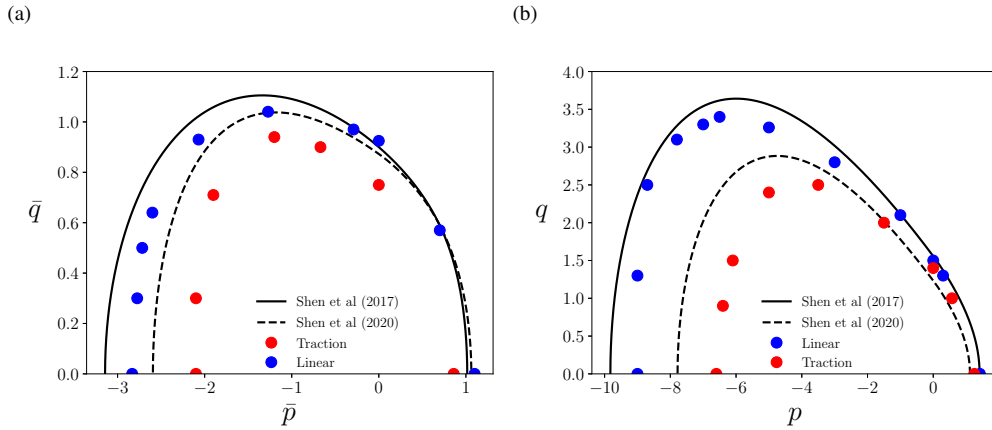
Figure 5. Comparison of the analytical expression (34) (Shen et al [33]) (solid line) and analytical yield surface provided by Shen et al [34] (dashed line) against the yield stresses obtained by employing the RVE with spherical void at the centre under linear and uniform traction boundary conditions. In-house finite finite element code results for two friction angles: (a) $\phi = 16.7°$ and (b) $\phi = 30.2°$.

6.1. Role of RVE boundary conditions

Virtual tests have first been performed for an RVE with a single spherical void in the centre of the RVE, while linear and uniform traction boundary conditions are considered, which are expected to provide upper and lower bound solutions, respectively, as discussed in Section 2.4.

Virtual testing results are generated by employing an implicit solution procedure and compared against analytical expression given in equation (34). Figures 5(a)

19

and 5(b) provide, respectively, a comparison between numerical and analytical results for two selected friction angles $\phi = 16.7°$ and $\phi = 30.2°$. It can be observed that virtual test results capture very well trends observed for the pressure sensitive elasto-plastic Drucker-Prager material, with linear boundary conditions providing an excellent agreement with analytical expression (34) provided by Shen et al [33]. However, it appears that a recently updated analytical expression given by Shen et al [34] provides an improved estimate of the yield criterion for porous elasto-plastic material with Drucker-Prager matrix, which fits within the upper and
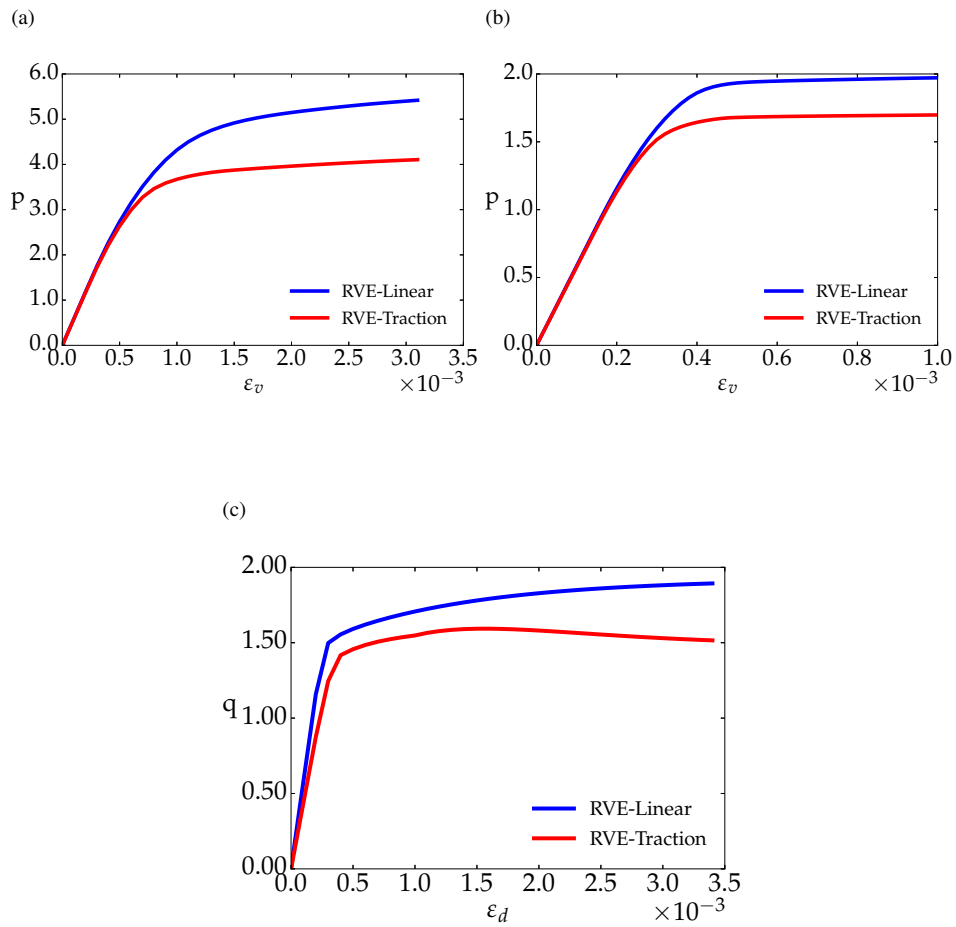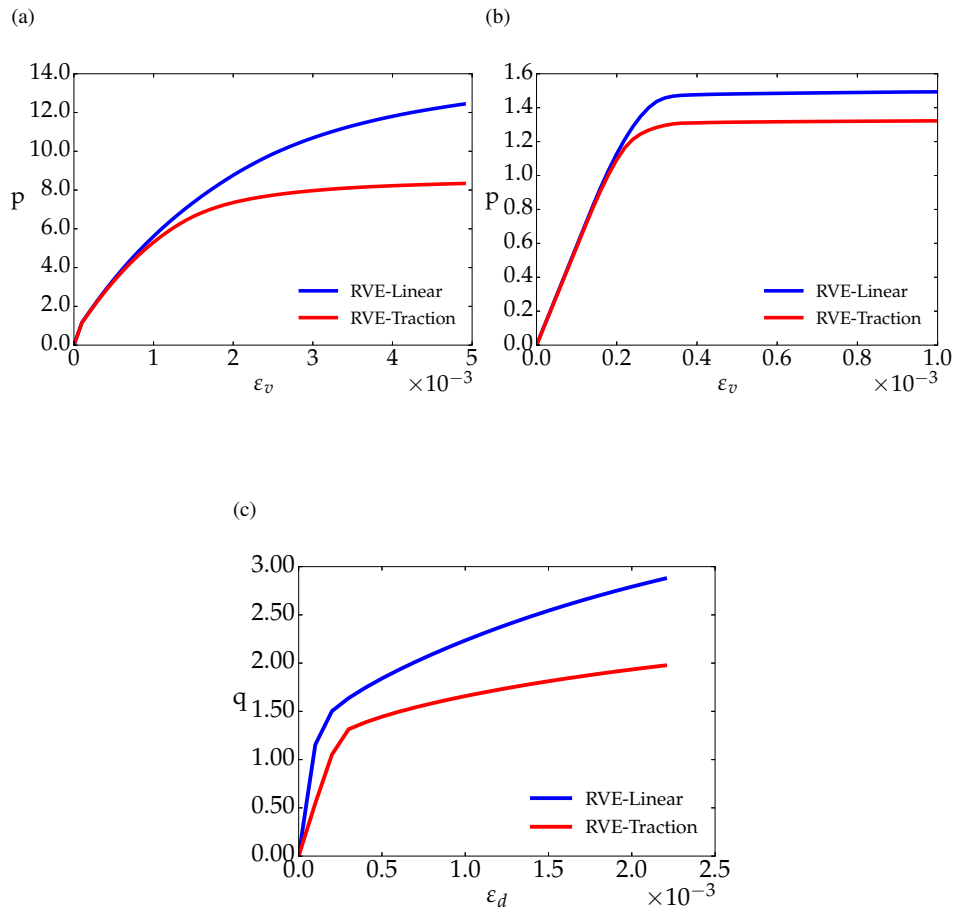

Figure 6. Stress-strain curves obtained by employing RVE with a spherical void under linear and uniform traction boundary conditions for $\phi = 16.7°$. Results are shown for three different loading conditions: (a) pure compression, (b) pure tension and (c) pure shear.

lower bound predictions associated with the FEM solutions obtained by employing linear and uniform traction boundary conditions, respectively.

Figures 6 and 7 depict stress-strain evolution diagrams for both friction angles $\phi = 16.7°$ and $\phi = 30.2°$, respectively. In particular, Figures 6(a), 6(b), 7(a) and 7(b) give $p - \varepsilon_v$ evolution diagrams for triaxial compression and tension, respectively, while Figures 6(c) and 7(c) give $q - \varepsilon_d$ for pure shear loading. The diagrams are used to identify yield stress for each loading combination, clearly illustrating the difficulty in selecting the appropriate value of the yield stress. They provide a justification for the use of Casagrande method as described in Section 5.2

(a)

(b)

(c)

Figure 7. Stress-strain curves obtained by employing RVE with a spherical void under linear and uniform traction boundary conditions for $\phi = 30.2°$. Results are shown for three different loading conditions: (a) pure compression, (b) pure tension and (c) pure shear.

21

to identify the yield stress within the virtual testing strategy. This is particularly evident on a stress-strain curve for frictional angle $\phi = 30.2°$, which, under pure compression loading conditions depicted in Figure 7(a), shows gradual transition from elastic to plastic regime without a clearly identifiable yield stress point.

6.2. Choice of RVE

In order to illustrate the influence that the choice of RVE may have on constructed yield surface the virtual testing procedure is in this section performed on different RVEs described in Section 5.1 and given in Figure 3. With a view to practical applications the virtual testing strategy described in Section 5 has been implemented in the commercial software ParaGeo.

Virtual testing results are generated by employing linear boundary condition, which has been shown in previous Section 6.1 to lead to the yield surface that is in very good agreement with analytical expressions. Figure 8 provides a comparison between numerically constructed yield surfaces and analytical expression (34) (Shen et al [33]) and expression provided by Shen et al [34] for two selected friction angles $\phi = 16.7°$ and $\phi = 30.2°$. It can be observed that virtual testing results show very good agreement with analytical expression for both choices of RVE, with no significant differences between RVEs with a single and multiple voids. The correspondence between virtual testing results and analytical expressions is particularly good for the smaller friction angle of $\phi = 16.7°$, as show in Figures 8(a) and 8(c). Notably, for friction angle $\phi = 30.2°$ the RVE with multiple voids provides slightly softer response than the RVE with a single void as can be observed by comparing Figures 8(b) and 8(d).

Figure 9 depict stress-strain evolution diagrams for friction angle $\phi = 30.2°$. Figure 9(a) and Figure 9(b) give $p - \varepsilon_v$ evolution diagrams for triaxial compression and tension, respectively, while Figure 9(c) gives $q - \varepsilon_d$ for pure shear loading. The stress-strain evolution is displayed for an RVE with a single void for both in-house implicit code and ParaGeo results, while results for RVE with multiple voids are based on ParaGeo simulation. Clearly, the stress-strain diagrams obtained by both codes are virtually indistinguishable. These diagrams provide typical stress-strain curves that are used to identify yield stress for each loading combination, again clearly illustrating the difficulty in selecting the appropriate value of the yield stress particularly for larger value of frictional angle $\phi = 30.2°$ under pure compression loading conditions shown in Figure 9(a). They provide further justification for the use of Casagrande method as described in Section 5.2 to identify the yield stress within the virtual testing strategy.
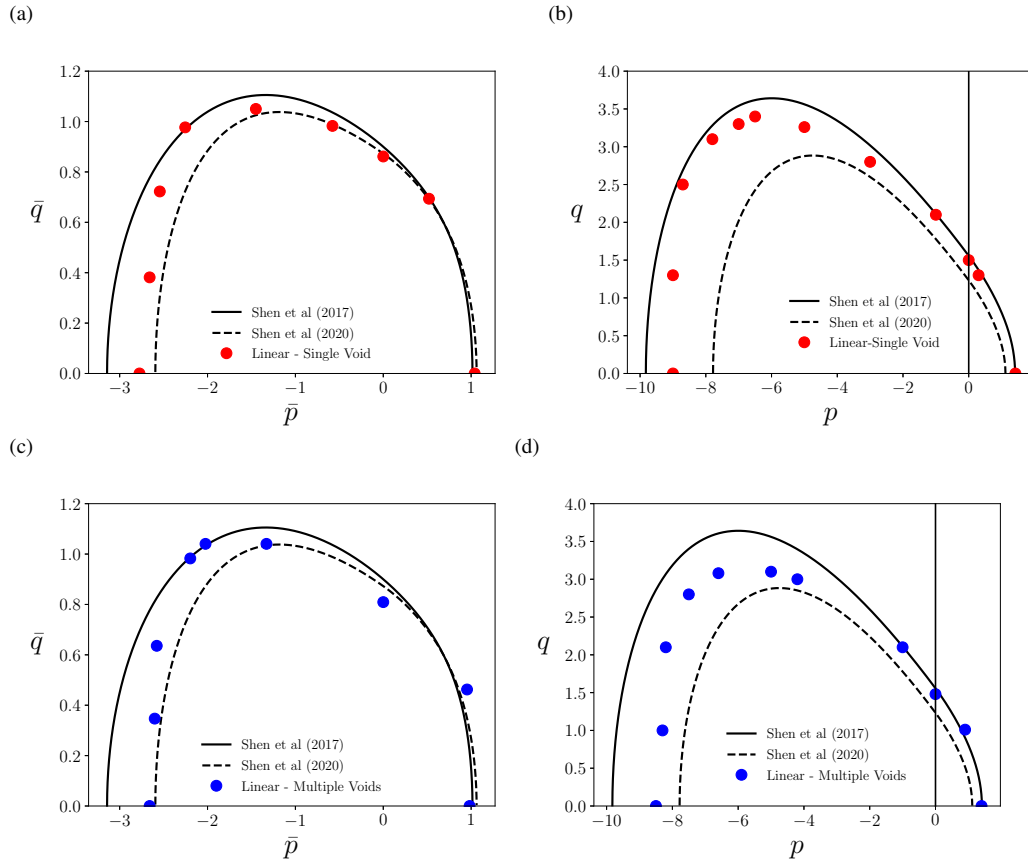
22

Figure 8. Comparison between yield surface given by analytical expression (34) (solid line), analytical yield surface provided by Shen et al [34] (dashed line) and numerical solutions: (a) and (c) display results for RVE with single void and eight voids, respectively, with the friction angle $\phi = 16.7°$; (b) and (d) show results for RVE with single void and eight voids, respectively, with the friction angle $\phi = 30.2°$. All results are obtained by employing ParaGeo.
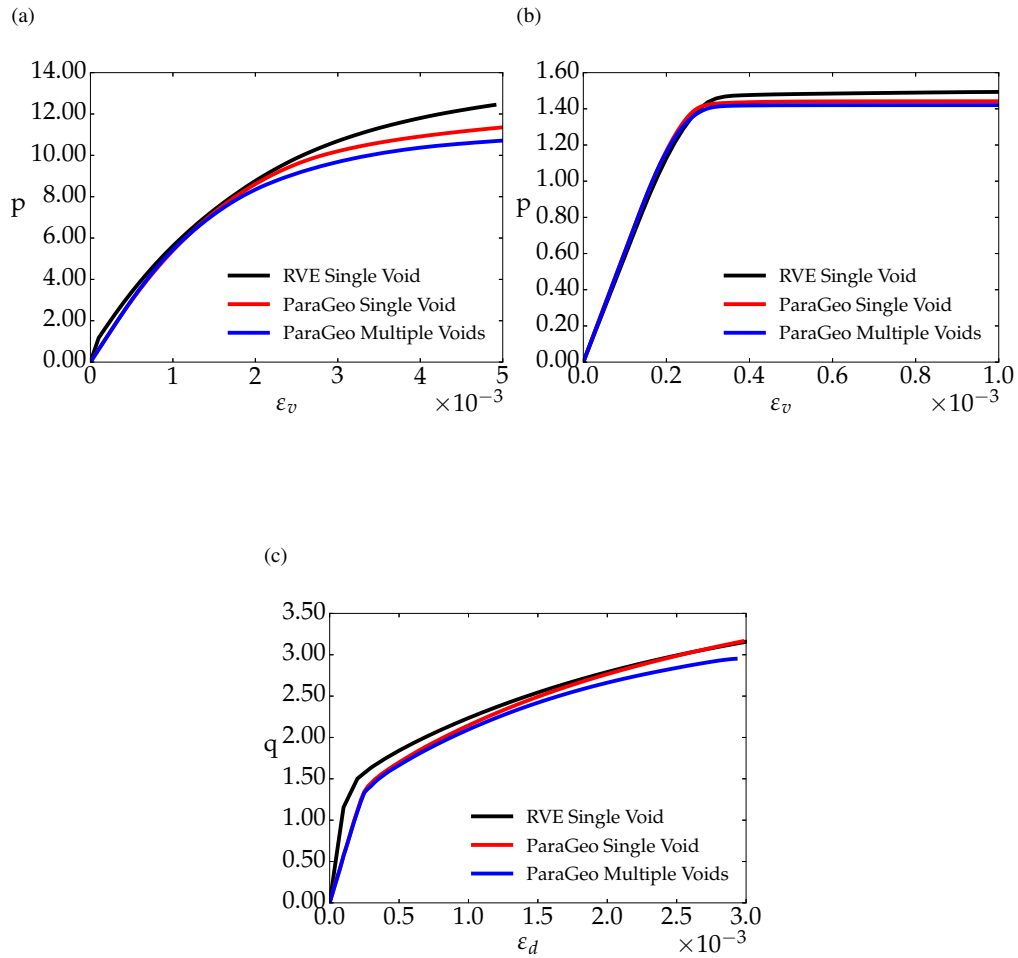
Figure 9. Stress-strain curves obtained by employing RVEs with a spherical void and multiple voids under linear boundary conditions for $\phi = 30.2°$. Results are shown for three different loading conditions: (a) pure compression, (b) pure tension and (c) pure shear.

6.3. *Mechanisms of plastic collapse*

In order to get an insight into mechanisms of plastic collapse for porous materials composed of pressure sensitive elasto-plastic matrix, the equivalent plastic strain distribution plots are depicted in Figures 10 and 11.

Figure 10 illustrates the effective plastic strain distribution for the RVEs with a single void, corresponding to the loads at which plastic collapse takes place. The results for the RVE with a single void shown in Figure 10 are obtained by imposing two kinematical constraints on the RVE: Figures 10(a), 10(c) and 10(e) depict equivalent plastic strain for linear, while Figures 10(b), 10(d) and 10(f) depict results for uniform traction boundary condition. Similar distributions of equivalent plastic strain can be observed for both linear and traction boundary conditions, however, the strains at which these levels have been achieved are lower for the uniform traction boundary conditions. This confirms that the uniform traction boundary conditions with minimal kinematical constrains provide a lower bound solution to the plastic collapse of the RVE as clearly illustrated in stress-strain diagrams given in Figures 6 and 7, and yield surface estimates shown in Figure 5.

It can be observed from Figure 11 that the plastic collapse for the triaxial loading conditions takes place by development of a plastic deformation in a layer of material surrounding the void (Figure 11(c)), which spreads to the boundary causing extensive plastification and collapse (Figure 11(d)). This failure pattern is clearly illustrated for triaxial compression in Figures 10(a) and 10(b) and for triaxial tension in Figures 10(c) and 10(d). For pure shear loading depicted in Figures 10(e) and 10(f), the failure pattern starts similarly by development of a plastic deformation in a layer of material surrounding the void, but then spreads diagonally to reach the boundary along the direction of principal tensile stress. This failure pattern is very clearly illustrated for the uniform traction boundary condition depicted in Figure 10(f), while the plastic zone appears more diffused for linear boundary condition shown in Figure 10(e).
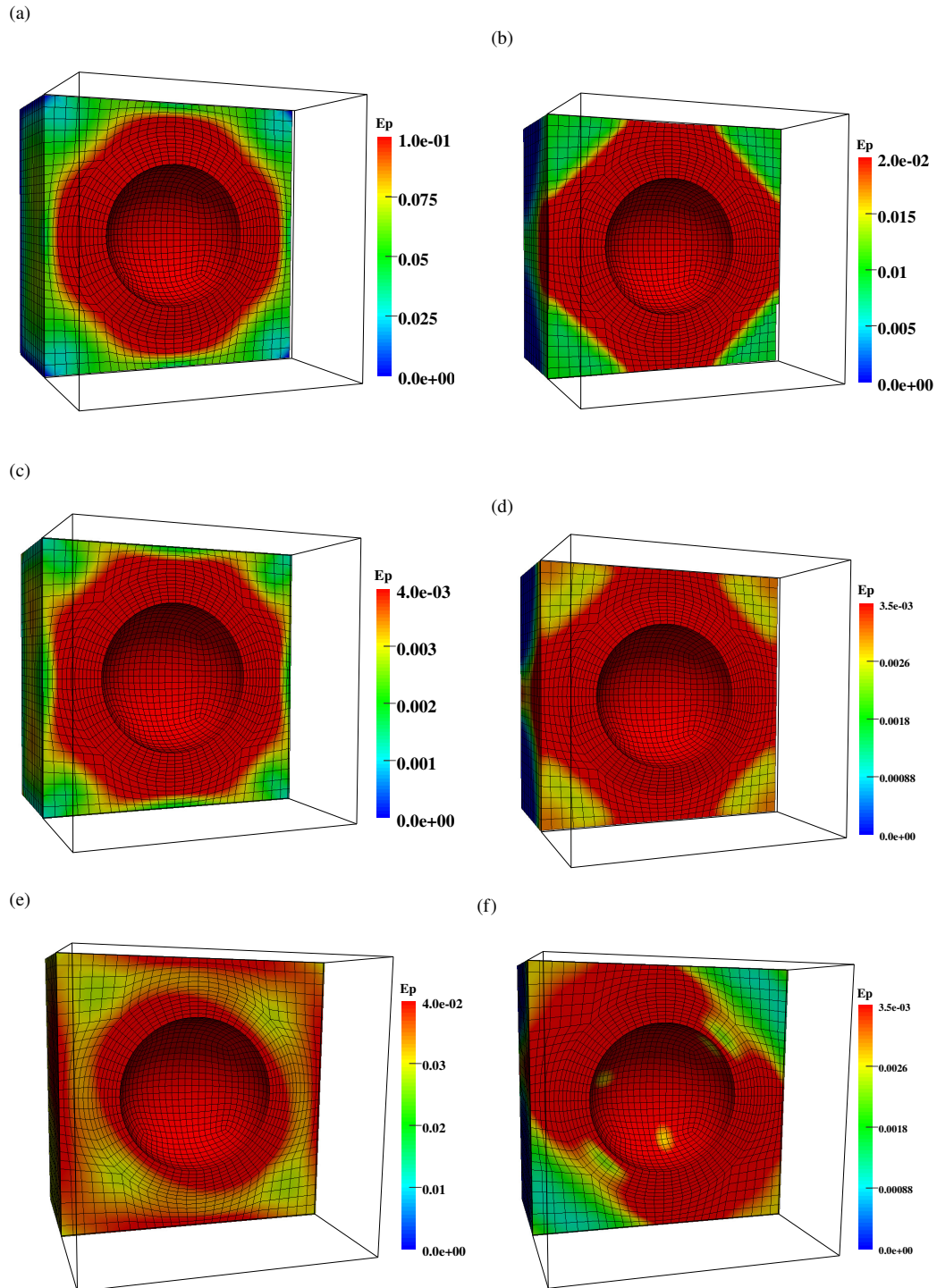
25

Figure 10. Evolution of equivalent plastic strain for the RVE with single void and friction angle $\phi = 16.7°$. (a), (c) and (e) display results under linear boundary condition, while (b), (d) and (f) display results under uniform traction boundary condition. (a)-(b) triaxial compression, (c)-(d) triaxial tension and (e)-(f) pure shear.
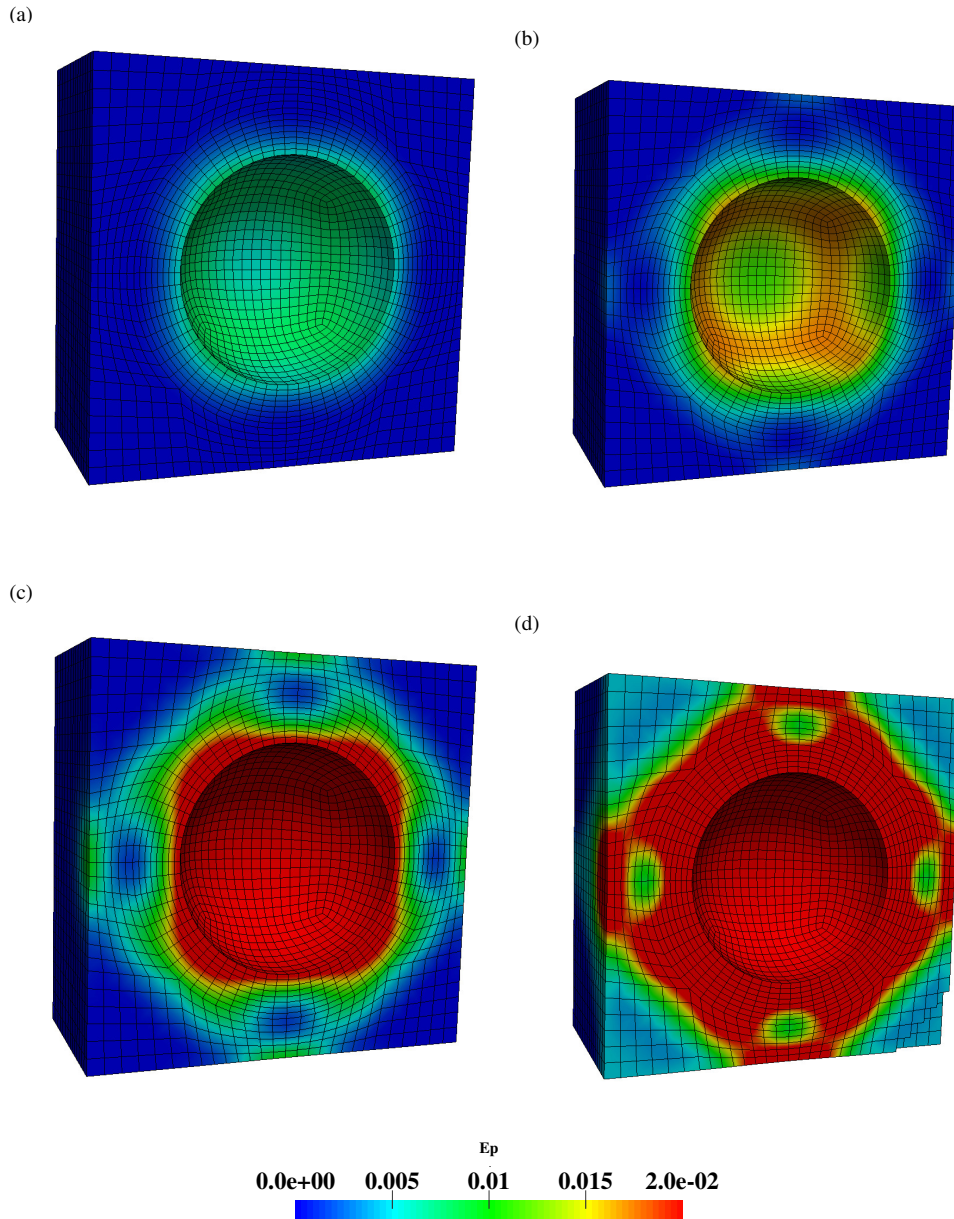
Figure 11. Evolution of equivalent plastic strain for the RVE with single void and friction angle $\phi = 16.7°$ under uniform traction boundary condition. Triaxial compression loading at different load levels: (a) 5% of the total load (b) 7% of the total load, (c) 10% of the total load, and (d) 20% of the total load .

7. Multi-scale material characterisation application

In order to provide a demonstration of the potential that virtual testing strategy described in Section 5 can have on practical applications, this section describes the application to the realistic soft rock sample. The virtual testing procedure is implemented in the commercial code ParaGeo [52] to allow simulation of large scale problems associated with complex heterogeneous rock microstructure. In order to provide more flexibility in the description of constitutive behaviour the SR4 constitutive model described in Section 4.3 is employed.

The SR4 model is an extension of the SR3 model proposed by Crook et al. [47], which has proved very successful in simulation of a wide range of problems from geological practice (see, e.g. [53; 46; 54]). The SR4 is a generic critical state model which includes non-associated hardening law and by the appropriate choice of material parameters can provide a close match to the porous Drucker-Prager type elasto-plastic material.

Figure 12(a) shows a digital image of a rock sample typical for a sandstone, which is composed of pressure sensitive elasto-plastic matrix and two types of elastic inclusion particles. Quartz_1 has Young's modulus of $E = 70000$ MPa, while softer Quartz_2 has Young's modulus of $E = 50000$ MPa. The matrix is composed of a porous elasto-plastic material characterized by SR4 constitutive model with Young's Modulus $E = 3000$ MPa, tensile intercept $p_t = 1.5$ MPa, pre-consolidation pressure $p_c = -3.2$ MPa and both friction ϕ and dilation angle ψ given as $\phi = \psi = 50°$. The Poisson's ratio $\nu = 0.3$ is used for all materials in the sample. The inclusion ratio of the sample stands at 17%. The discretised model depicted in Figure 12(b) is meshed with 65648 triangular elements.

Figure 13 depicts stress-strain evolution diagrams under different loading conditions. Figure 13(a) and Figure 13(b) give $p - \varepsilon_v$ evolution diagrams for compression and tension loading, respectively, while Figure 13(c) give $q - \varepsilon_d$ for pure shear loading. The diagrams Figures 13(a) to 13(c) provide typical stress-strain curves that are used to identify yield stress for each loading combination, again clearly illustrating the importance of using the Casagrande method described in section 5.2 to identify the yield stress within the virtual testing strategy.

Figure 14 illustrates the effective plastic strain distribution corresponding to the loads at which plastic collapse takes place. It can be observed from Figures 14(a) and 14(b) that the plastic collapse for both compression and tension dominated loading conditions takes place by development of large plastic deformations at the
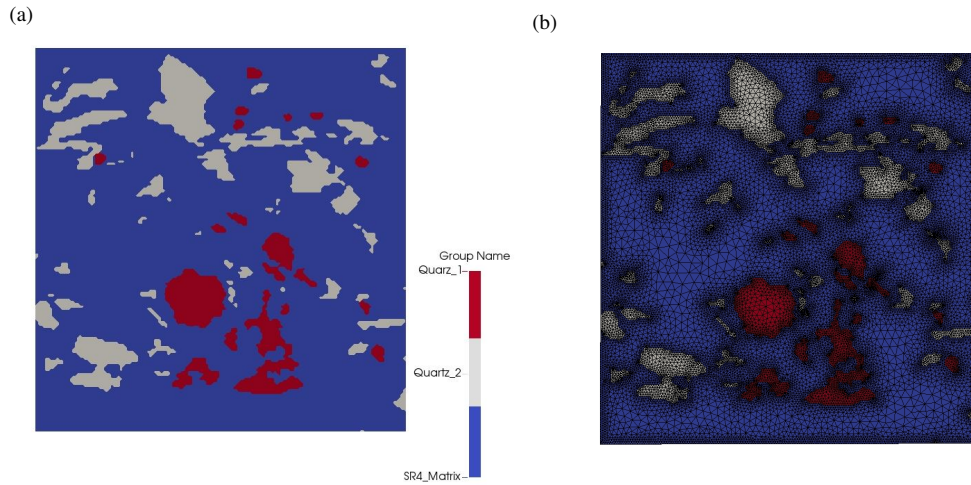
Figure 12. Sandstone RVE: (a) digital image, (b) finite element mesh.

interface between hard particles and soft rock matrix, which then spreads to the boundary leading to extensive plastification and rock sample collapse. For shear loading depicted in Figure 14(c), the failure pattern starts similarly by development of a plastic deformation at the interface between hard particles and soft rock matrix, but then spreads by formation of shear bands that reach the boundary leading to plastic collapse.

Figure 15 depicts a set of yield points recovered by virtual testing procedure and numerically constructed yield surface. The yield surface is obtained by employing the SR4 constitutive model and an appropriate choice of material parameters that provides the best fit to the set of yield points. The yield surface constructed in such a way defines the meso-scale type constitutive model, which, within the virtual testing strategy - type B (see Figure 2), provides a constitutive model to be used for numerical simulations at the macro-scale.
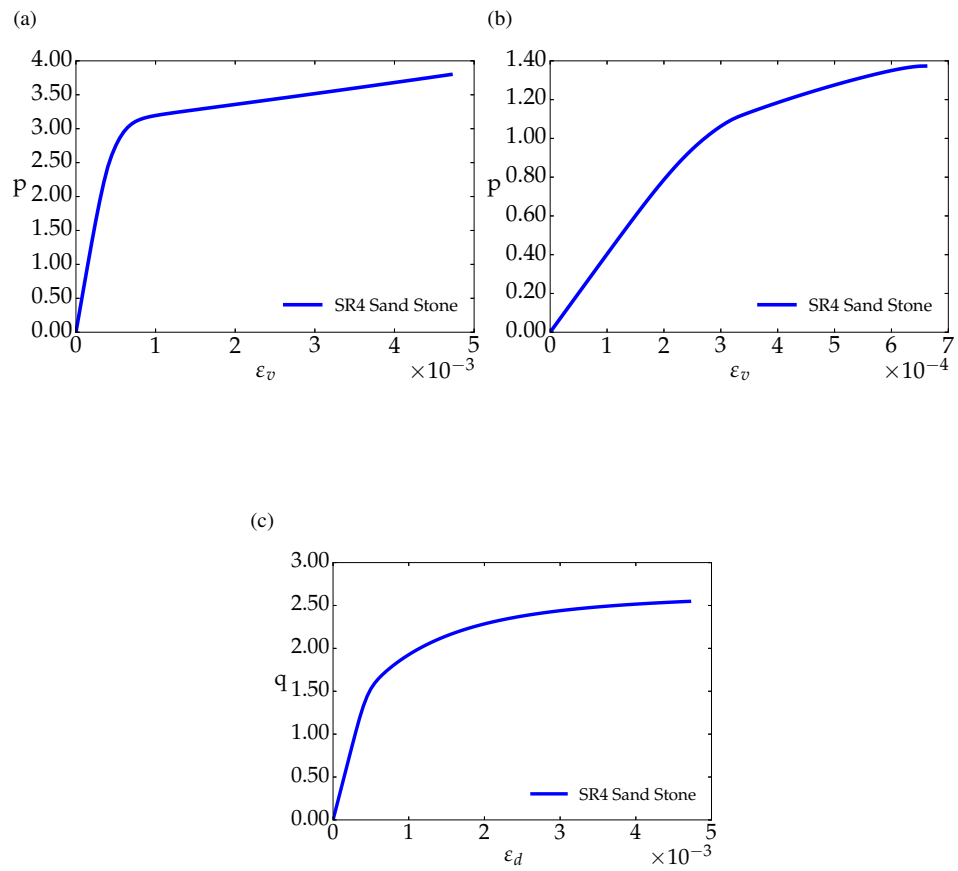
29

Figure 13. Stress-strain curves of the sandstone RVE under different loading conditions: (a) compression, (b) tension and (c) shear.
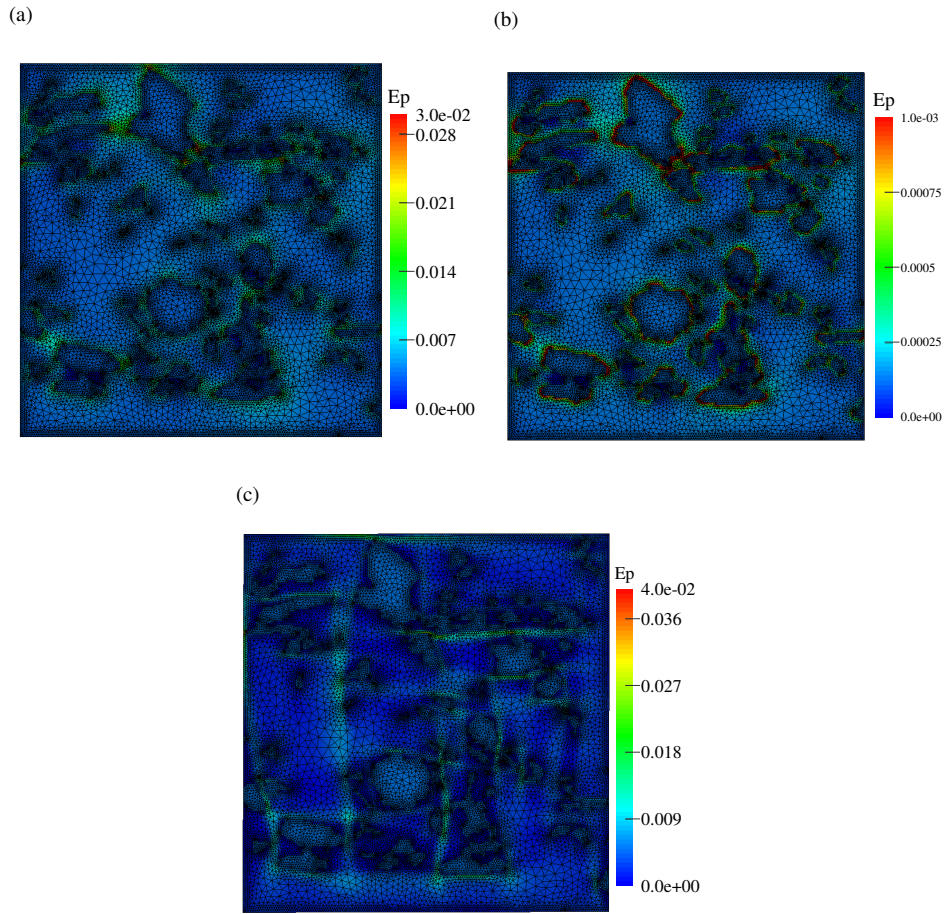
Figure 14. Equivalent plastic strain distribution for the sandstone RVE under different loading conditions: (a) compression, (b) tension and (c) shear.
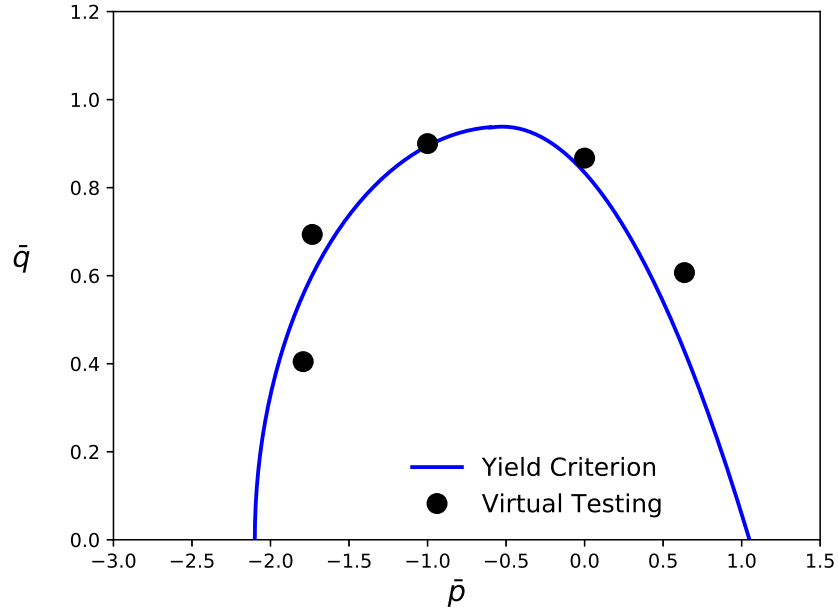
Figure 15. Set of yield stress points together with yield surface constructed by the virtual testing procedure.

8. Concluding remarks

Virtual testing strategy has been developed in this work based on computational homogenisation approach following a unified variational formulation. The potential of the strategy is illustrated by performing estimate of the effective properties of porous solid with elasto-plastic Drucker-Prager matrix. Excellent correspondence has been demonstrated between the computationally generated effective yield criteria for porous solids and the recently proposed analytical estimates for Drucker-Prager type solids and the SR4 constitutive model for soft rocks.

An important feature of the proposed virtual testing strategy is use of the Casagrande procedure [51] to identify yield points and thus to construct an effective yield surface for heterogeneous elasto-plastic materials. This procedure is commonly employed in experimental characterisation of geological materials that invariably display appreciable pressure sensitivity. A range of numerical tests performed in this work demonstrates that the virtual testing strategy enhanced by the Casagrande procedure provides an efficient and accurate methodology for constructing yield surface for a wide range of realistic geological materials.

The virtual testing procedure has been implemented in the commercial code ParaGeo [52] to allow simulation of large scale problems associated with complex heterogeneous rock microstructures. In order to illustrate the potential that the developed virtual testing strategy may have on characterisation of practically relevant materials, the effective yield surface has been constructed for the realistic soft rock sample based on a digital image of a sandstone.

References

[1] J. C. Jaeger, N. G. W. Cook, and R. W. Zimmerman. *Fundamentals of Rock Mechanics*. Blackwell Publishing, Oxford, Fourth edition, 2007.

[2] Y. J. Cao, W. Q. Shen, J. F. Shao, and N. Burlion. Influences of micro-pores and meso-pores on elastic and plastic properties of porous materials. *Eur. J. Mech. A/Solids*, 72:407–423, 2018.

[3] G. L. Manjunath and B. Jha. Geomechanical characterization of gondwana shale across nano-micro-meso scales. *Int. J. Rock. Mech. Min. Sci.*, 119: 35–45, 2019.

[4] Y. Zhao, Y. Wang, W. Wang, W. Wan, and J. Tang. Modeling of non-linear rheological behavior of hard rock using triaxial rheological experiment. *Int. J. Rock. Mech. Min. Sci.*, 93:66–75, 2017.

[5] X. L. Xu and M. Karakus. A coupled thermo-mechanical damage model for granite . *Int. J. Rock. Mech. Min. Sci.*, 103:195–204, 2018.

[6] P M. Suquet. Local and global aspects in the mathematical theory of plasticity. In A. Sawczuk, editor, *Plasticity Today: Modelling Methods and Applications*. Elsevier Applied Science Publishers, Amsterdam, 1985.

[7] P M. Suquet. Elements of homogenization for inelastic solid mechanics. In E. Sanchez-Palencia and A. Zaoui, editors, *Elements of Homogenization for Inelastic Solid Mechanics*. Springer-Verlag, Berlin, 1987.

[8] S. Ghosh, K Lee, and S Murthy. Two scale analysis of heterogeneous elastic-plastic materials with asymptotic homogenization and voronoi cell finite element method. *Comp. Meth. Appl. Mech. Engng.*, 132:63–116, 1996.

[9] H. Moulinec and P. Suquet. A numerical method for computing the overall response of nonlinear composites with complex microstructure. *Comput. Meth. Appl. Mech. Engng.*, 157:69–94, 1998.

[10] J C. Michel, H. Moulinec, and P Suquet. Effective properties of composite materials with periodic microstructure: A computational approach. *Comp. Meth. Appl. Mech. Engng.*, 172:109–143, 1999.

[11] F. Feyel and J-L Chaboche. Fe^2 multiscale approach for modelling the elastoviscoplastic behaviour of long fibre SiC/Ti composite materials. *Comp. Meth. Appl. Mech. Engng.*, 183:309–330, 2000.

[12] C. Miehe, J. Schotte, and J. Schröder. Computational micro-macro transitions and overall tangent moduli in the analysis of polycrystals at large strains. *Comput. Materials Sci.*, 16:372–382, 1999.

[13] C. Miehe, J. Schröder, and J. Schotte. Computational homogenization analysis in finite plasticity. simulation of texture developtment in polycrystalline materials. *Comput. Meth. Appl. Mech. Engng.*, 171:387–418, 1999.

[14] C. Miehe and A. Koch. Computational micro-to-macro transitions of discretized microstructures undergoing small strains. *Arch. Appl. Mech.*, 72: 300–317, 2002.

[15] V. G. Kouznetsova, W. A. M. Brekelmans, and F. P. T. Baaijens. An approach to micro-macro modelling of heterogeneous materials. *Comput. Mech.*, 27: 37–48, 2001.

[16] P. Ladevèze, O. Loiseau, and D. Dureisseix. A micro-macro and parallel computational strategy for highly heterogeneous structures. *Int. J. Numer. Meth. Engng.*, 52:121–138, 2001.

[17] K. Terada and N. Kikuchi. A class of general algorithms for multi-scale analyses of heterogeneous media. *Comput. Meth. Appl. Mech. Engng.*, 190: 5427–5464, 2001.

[18] A. Ibrahimbegović and D Markovič. Strong coupling methods in multi-phase and multi-scale modeling of inelastic behavior of heterogeneous structures. *Comp. Meth. Appl. Mech. Engng.*, 192:3089–3107, 2003.

[19] A L Gurson. Continuum theory of ductile rupture by void nucleation and growth: Part 1 - yield criteria and flow rules for porous ductile media. *J. Eng. Mater. Technol.*, 99:2–15, 1977.

[20] A. A. Benzerga and J.-B. Leblond. Ductile fracture by void growth to coalescence. *Adv. Appl. Mech.*, 44:169–305, 2010.

[21] F. Fritzen, S. Forest, T. Böhlke, D. Kondo, and T Kanit. Computational homogenization of elasto-plastic porous metals. *Int. J. Plasticity*, 29:102–119, 2012.

[22] V. Monchiet and G Bonnet. Gurson-type model accounting for void size effects. *Int. J. Solids Struct.*, 50:320–327, 2013.

[23] C. Ling, J. Besson, S. Forest, B. Tanguy, F. Latourte, and E. Bosso. An elastoviscoplastic model for porous single crystals at finite strains and its assessment based on unit cell simulations. *Int. J. Plasticity*, 84:58–87, 2016.

[24] O. Cazacu and B. Revil-Baudard. New analytic criterion for porous solids with pressure-insensitive matrix. *Int. J. Plasticity*, 89:66–84, 2017.

[25] M. I. El Ghezal and I. Doghri. Porous plasticity: Predictive second moment homogenization models coupled with Gurson's single cavity stress-strain solution. *Int. J. Plasticity*, 108:201–221, 2018.

[26] H Y Jeong. A new yield function and a hydrostatic stress-controlled model for porous solids with pressure-sensitive matrices. *Int. J. Solids Struct.*, 39: 1385–1403, 2002.

[27] T F. Guo, J. Faleskog, and C Shih. Continuum modeling of a porous solid with pressure-sensitive dilatant matrix. *J. Mech. Phys. Solids*, 56:2188–2212, 2008.

[28] D. Durban, T. Cohen, and Y Hollander. Plastic response of porous solids with pressure sensitive matrix. *Mech. Res. Commun.*, 37:636–641, 2010.

[29] J. Pastor, P. Thoré, and F Pastor. Limit analysis and numerical modeling of spherically porous solids with Coulomb and Drucker-Prager matrices. *J. Comput. Appl. Math.*, 234:2162–2174, 2010.

[30] V. Monchiet and D Kondo. Exact solution of a plastic hollow sphere with a Mises-Schleicher matrix. *Int. J. Eng. Sci.*, 51:168–178, 2012.

[31] F. Pastor, D. Kondo, and J. Pastor. 3D-FEM formulations of limit analysis methods for porous pressure-sensitive materials. *Int. J. Num. Meth. Engng.*, 95:847–870, 2013.

[32] W Q. Shen, J F. Shao, D. Kondo, and G De Saxce. A new macroscopic criterion of porous materials with a Mises-Schleicher compressible matrix. *Eur. J. Mech. A/Solids*, 49:531–538, 2015.

36

[33] W Q. Shen, J. Zhang, J F. Shao, and D Kondo. Approximate macroscopic yield criteria for Drucker-Prager type solids with spheroidal voids. *Int. J. Plasticity*, 99:221–247, 2017.

[34] W Q. Shen, J F. Shao, Z B. Liu, A. Oueslati, and G De Saxcé. Evaluation and improvement of macroscopic yield criteria of porous media having a Drucker-Prager matrix. *Int. J. Plasticity*, 126:102609, 2020.

[35] E A. de Souza Neto and R A Feijóo. Variational foundations of multi-scale constitutive models of solid:small and large strain kinematical formulation. Technical Report No. 16/2006, National Laboratory for Scientific Computing (LNCC/MCT), Brazil, 2006.

[36] D. Perić, E A. de Souza Neto, R A. Feijóo, M. Partovi, and A J Carneiro Molina. On micro-to-macro transitions for multi-scale analysis of non-linear heterogeneous materials:unified variattional basis and finite element implementation. *Int. J. Num. Meth. Engng.*, 87:149–170, 2011.

[37] S M. Giusti, P J. Blanco, E A. de Souza Neto, and R A Feijóo. An assessment of the Gurson yield criterion by a computational multi-scale approach. *Eng. Comput.*, 26:281–301, 2009.

[38] D D. Somer, D. Perić, E A. de Souza Neto, and W G Dettmer. Yield surfaces of heterogeneous media with debonded inclusions. *Eng. Comput.*, 32:1802–1813, 2015.

[39] P C. Rodrigo, L I A. Rodrigues, and F M Andrade Pires. Prediction of the yielding behaviour of ductile porous materials through computational homogenization. *Eng. Comput.*, 35:604–621, 2017.

[40] H. Zhang, M. Diehl, F. Roters, and D. Raabe. A virtual laboratory using high resolution crystal plasticity simulations to determine the initial yield surface for sheet metal forming operations. *Int. J. Plasticity*, 80:111–138, 2016.

[41] A. Esmaeili, S. Asadi, F. Larsson, and K. Runesson. Construction of macroscale yield surfaces for ductile composites based on a virtual testing strategy. *Eur. J. Mech. A/Solids*, 77:103786, 2019.

[42] D D. Somer, E A. de Souza Neto, D. Perić, and W G Dettmer. A sub-stepping scheme for multi-scale analysis of solids. *Comput. Meth. Appl. Mech. Engng.*, 198:1006–1016, 2009.

[43] R. Hill. A new macroscopic criterion of porous materials with a Mises-Schleicher compressible matrix. *J. Mech. Phys. Solids*, 13:213–22, 1965.

[44] J. Mandel. *Plasticité Classique et Viscoplasticité*. CISM Courses and Lectures No. 97. Springer-Verlag, Udine, Italy, 1971.

[45] E A. de Souza Neto, D. Peric, and D R J Owen. *Computational Methods for Plasticity: Theory and Applications*. Wiley, Chichester, 2008.

[46] J. Obradors-Prats, M. Rouainia, A C. Aplin, and A J L Crook. Assessing the implications of tectonic compaction on pore pressure using a coupled geomechanical approach. *Marine Petroleum Geol.*, 79:31–43, 2017.

[47] A J L. Crook, S M. Willson, J G. Yu, and D R J Owen. Predictive modelling of structure evolution in sandbox experiments. *J. Struct. Geol.*, 28:729–744, 2006.

[48] D Muir Wood. *Soil Behaviour and Critical State Soil Mechanics*. Cambridge University Press, Cambridge, 1990.

[49] M. Rouainia and D Muir Wood. An implicit constitutive algorithm for finite strain cam clay elasto-plastic model. *Mech. Cohesive-Frictional Mater.*, 6:469–489, 2000.

[50] S. Ahmed, T.M. Müler, M. Madadi, and V. Calo. Drained pore modulus and Biot coefficient from pore-scale digital rock simulations. *Int. J. Rock. Mech. Min. Sci.*, 114:62–70, 2019.

[51] A. Casagrande. The determination of the pre-consolidation load and its practical significance. In *Proceedings of the 1st International Conference on Soil Mechanics and Foundation Engineering*, volume 3, pages 60–64, Harvard University, Cambridge, 1936.

[52] A J L Crook. ParaGeo: A Finite element model for coupled simulation of the evolution of geological structures. Technical report, Three Cliffs Geomechanical Analysis, Swansea, UK, 2013.

[53] D. A. Thornton and A. J. L. Crook. Predictive Modeling of the Evolution of Fault Structure: 3-D Modeling and Coupled Geomechanical/Flow Simulation. *Rock Mech Rock Eng*, 47:1533–1549, 2014.

[54] J. Obradors-Prats, M. Rouainia, A. C. Aplin, and A. J. L. Crook. A diagenesis model for geomechanical simulations: Formulation and implications for pore pressure and development of geological structures. *Journal of Geophysical Research: Solid Earth*, 124:4452–4472, 2019.